Article:

Wan, Q., Farr, N.T.H., Li, P. et al. (2024) Carbon nanotubes facilitate silk hierarchical assembly by dry drawing. Small Structures, 5 (4). 2300435. ISSN: 2688-4062

https://doi.org/10.1002/sstr.202300435

Carbon Nanotubes Facilitate Silk Hierarchical Assembly by Dry Drawing

Quan Wan, Nicholas T. H. Farr, Peng Li, Darren Batey, Christoph Rau, John Rodenburg, Leihao Lu, Peter R. Laity, Zongpu Xu, Chris Holland, Cornelia Rodenburg,* and Mingying Yang**

Biologically derived hierarchical structural materials not only boast energy-efficient processing but also exhibit impressive mechanical performance. Silk stands as the gold standard in hierarchical fiber production, leveraging a unique combination of advantages. Nevertheless, the artificial replication of silk poses technical challenges related to precision processing and comprehensive molecular control. To address such issues, this study investigates the hierarchical assembly of solid regenerated silk in an air atmosphere, facilitated by the incorporation of carbon nanotube (CNT) seeding. Results obtained highlight that this CNT seeding facilitates multiscale structure development in response to post-spin tensile stress. Such CNT bridged structure assembly bypasses some natural processing control variables (pH, ions) and the necessary solvent immersed state for conventional silk post-drawing. Combining secondary electron hyperspectral imaging and 3D synchrotron X-ray ptychotomography, this study reports silk protein conversion from a disordered as-spun state to a longitudinal orientated semi-crystalline nano structure during drawing. The development of microscale structure during the drawing process is attributed to the presence of CNTs, yielding mechanical properties comparable to, and frequently surpassing, those exhibited by native fibers. These findings collectively propose a framework for exploring novel processing routes and offer a practical means controlling self-assembly in silk materials.

1. Introduction

A hallmark of silk is the development of a complex hierarchical structure in response to flow processing. In vivo silk is spun via a protein denaturation pathway that includes ion concentration variation,[1] pH manipulation,[2] and is fueled by a flow-based "rate of work" energy input.[3] The resulting self-assembled fiber structures typically consist of ordered β-sheet dominated nanofibrils, a disordered amorphous matrix, and a meta-phase.[4] Combination of these components provides excellent extensibility while maintaining moderate tensile modulus, all serve to underpin a silk fiber's remarkable mechanical properties which are a unique combination of high strength and toughness.

Interestingly, silk's response to flow processing does not stop once spun. A multitude of studies on a range of natural and artificial silk fibers have clearly identified that post-draw processing is an effective means to improve mechanical properties through increased molecular alignment, crystallization, and decreased fiber diameter.[5–7] Yet, how silks reconfigure in response to this imposed tensile stress and subsequent plastic deformation has not been fully elucidated, especially for artificial silks which often fail before yielding.

This is attributed to artificial silk-based fibers typically being formed from either regenerated silk proteins,[8] redissolved from naturally spun silk fibers, or recombinant proteins inspired by natural silk protein sequences.[9] The creation of such fiber feedstocks is technically challenging. And often key elements of the natural silk proteins, such as their chain length or chemical responsiveness, can be lost during the process. To compensate for this deficiency, post-draw steps and immersion in organic

---

Q. Wan, L. Lu, Z. Xu, M. Yang
College of Animal Science
Zhejiang University
Hangzhou 310058, China
E-mail: yangm@zju.edu.cn

The ORCID identification number(s) for the author(s) of this article can be found under https://doi.org/10.1002/sstr.202300435.

DOI: 10.1002/sstr.202300435

N. T. H. Farr, P. R. Laity, C. Holland, C. Rodenburg
Department of Material Science and Engineering
University of Sheffield
Sheffield S1 3JD, UK
E-mail: christopher.holland@sheffield.ac.uk; c.rodenburg@sheffield.ac.uk

P. Li, D. Batey, C. Rau
Diamond Light Source Ltd.
Harwell Science and Innovation Campus
Didcot OX11 0DE, UK

J. Rodenburg
Department of Electronic and Electrical Engineering
University of Sheffield
Sheffield S1 3JD, UK

solvents (i.e., directed-assembly) are generally applied to artificial silk-based fibers to improve their mechanical properties.[10,11] However, this is somewhat of an energetic blunt instrument in comparison to the finesse of natural spinning.

This study investigates the incorporation of carbon nanotubes (CNTs) into an artificial silk feedstock, in a bid to mitigate the detrimental effects associated with silk regeneration. Additionally, facilitating the circumvention of the biomimetically challenging pH and ion chemical control elements inherent in native silk spinning. This has enabled the assembly of hierarchical structures in simple dry post drawing, and thus produces fibers with mechanical properties comparable to nature. Investigating fiber microstructure using a combination of 2D focused ion beam/scanning electron microscopy (FIB/SEM),[12] secondary electron hyperspectral imaging (SEHI),[13] and synchrotron ptychographic X-ray computed tomography[14] confirming a previous hypothesis of a progressive stress-induced phase transition in silks which enables structure development through gelation, fibrillation, and consolidation.[15]

The considered hypothesis for this study is that, at the nanoscale, the presence of CNTs facilitates heightened interactions among protein chains. This results in a significant increase in viscosity, enabling the absorption and conversion of a critical "rate of work" into a stress-induced phase transition. Furthermore, providing evidence suggesting that the CNT surface acts as a platform for subsequent microscale structure development and self-assembly via the recently proposed compartment-to-fibril transition model of Eliaz et al.[16] The resulting feedstock is able to undergo "ductless" spinning, in air, with fibers responding to draw in a similar manner to their natural counterparts in in vivo, thus demonstrating a strain-rate dependency on mechanical properties and strengths matching, if not exceeding, those of native silk fibers.

2. Results and Discussion

There are several examples where silk has been combined with low-dimensional materials,[17–20] and while sometimes controversial in their nature,[21–23] findings from these studies have typically centered on the end product rather than the assembly process itself. In contrast to prior research, this study tracks the process of structure formation and visually captures the progression toward the final assembly of hierarchical structures. **Figure 1** demonstrates that through the incorporation of CNTs into a regenerated silk feedstock, it becomes possible to prevent premature breakage in an air environment. Subsequently, allowing for the systematic and repeatable exploration of the post-yield behavior of artificial fibers. This approach allows us to capture a snapshot of stress induced structure development as it occurs, rather than inferring from before and after timepoints.

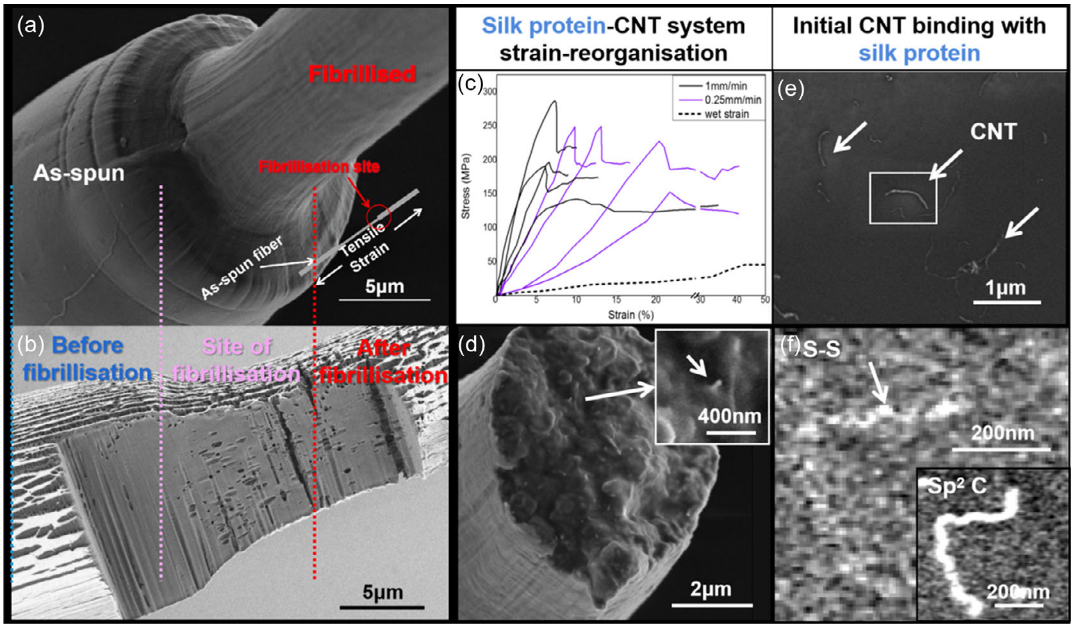

Figure 1. Regenerated silk-CNT fibers can withstand post-yield drawing processes in air due to silk-CNT interactions. a) "As-spun silk"-CNT fibers demonstrate necking when exposed to further tensile forces in air. b) Internal pockets appear at the necking site as revealed by FIB/SEM. c) Necking/tapering only occurs when the "as-spun fiber" reaches its yield point at strain rates below 2 mm min^{-1}; d) globular objects and drawn out CNTs can be observed within the stress fracture surface of a fibrillized fiber when inspected by SEM, exposed CNT is drawn out and differ from globular objects as highlighted by yellow arrow; e) it is considered by the authors that this process is enabled by protein-CNT interfacial binding; SEM of a spin-cast aqueous silk-CNT system shows an interfacial layer surrounding CNTs. The protein attachment is supported by the presence of bright patches along the CNTs as these patches are wider than the original CNT diameter (see Supporting Information). This image is backscattered SEM image, thus bright appearance is also likely caused by increased density. f) SEHI maps providing evidence of a spatial localization of an increased electron emission in the disulfide bond (S—S) energy window within the silk protein (white arrow) neighboring to locations identified as sp^2-carbon signal, thus originating from the (CNT) suggest the interfacial layer is formed by silk protein bonding to CNTs.

The SEM image presented in Figure 1a illustrates that the as-spun silk protein-CNT system can withstand a post-draw in air, with the necking site identified by a diameter reduction. Fibrillar structures appear on the surface in sections of reduced diameter, indicating higher stress. Upon further inspection, multiple necking/fibrillization sites (see S1, Supporting Information) can exist in one drawing process. These simultaneous necking result in a fibrillized fiber of uniform diameter when post-drawing is completed (Figure S1, Supporting Information). Notably, none of the fibrillization behavior in dry air was possible in feedstocks without CNTs present as their spun fibers broke prematurely.[24]

FIB milling revealed elongated pockets emerged precisely at the necking site (Figure 1b). The application of FIB is known to produce artefact aligned to ion beam orientation on the milling section, such as the line feature perpendicular to fiber observed in this image. However, in contrast to the vertical lines caused by ion beam milling, these pocket structures are perpendicular to ion beam, thus is not ion beam milling artefacts. This result is confirmed by S2, Supporting Information, and synchrotron X-ray ptychotomography (presented later) and was previously observed in silk spinning.[15] Importantly, these pockets are aligned to the fiber axis and their anisotropy increases further away from the necking site, suggesting they are responding to the bulk mechanical deformation (extensional plastic flow) of the fiber. The location and shape of these pockets at the point of drawdown are extremely informative, as the drawdown itself bears a striking resemblance to the internal drawdown taper seen in natural silk ducts.

Originally reported by Knight and Vollrath,[25] the position of the draw down taper, the point at which silk feedstock appears to pull away from the walls of the duct without a significant change in duct diameter, is also related to the speed at which silk is produced, or reeled, from the animal, with a retreating of the position further up the duct as reeling speed increased. This suggests that tapering is a response to a critical stress threshold being reached via the spinning forces being applied to the feedstock.

In further support that the tapering seen in the CNT-regenerated silk system is a response to a critical stress threshold, it is noted that tapering only occurs after the yield stress of these "as-spun" fibers is exceeded (Figure 1c) and for fibers spun in air at strain rates below 2 mm min^{-1} and under dry conditions, which suggests a maximum rate of work input capacity for these materials.[3,26] The observed yield stress levels for these fibers are between 70 and 150 MPa, regardless of Young's modulus, which overlaps with reported yield stress 50–250 MPa values for *B. mori* silk[27] (from which the regenerated silk protein is extracted). Thus, it associates the bulk yield stress with the force needed to initiate necking and subsequent fibrillization in the fiber.

SEM inspection of cross sections of fractured surfaces of fibrillized fibers such as those shown in Figure 1d reveals an uneven fracture surface containing nanoscale globular structures (diameter ≈50 nm) and drawn out CNT distributed across the fiber. Previous SEM analysis on degummed silk fiber fracture surfaces has shown similar globular structures ≈100 nm in diameter. Atomic force miscroscope (AFM) longitudinal sections of these features[28] revealed that these globules were indeed 1–2 μm nanofibrils that align approximately along the fiber axis.[29] Notably, such ≈100 nm globules have also been observed in sections of spider silks.[30] Thus, the fiber section appears identical to natural hierarchical silk fiber. The only structural difference is the drawn out CNT, since silk nanofibril itself cannot be drawn out from the fiber matrix phase. Together from the observations of pockets, necking and globules in response to an externally applied stress field support the view that this CNT-regenerated silk system can access nature's stress-induced phase separation pathway for hierarchical structure development.[31]

These obtained results suggest that the presence of CNTs facilitates the accumulation of sufficient stress for necking during the draw process. The interaction between silk proteins and CNTs is evident from the initial dispersion process of CNTs into the regenerated silk solution. Dispersion was achieved through the use of LiBr and sonication, as this solvent state promotes an amorphous "worm-like" extended conformation of the silk proteins,[32] exposing potential adhesion sites to CNTs, whilst also preventing protein-protein aggregation[33] prior to subsequent LiBr removal via dialysis to produce an aqueous regenerated silk protein-CNT solution for experimentation.

Low voltage scanning electron microscope (LV SEM) images collected with a backscatter detector of films cast from the CNT-regenerated silk system revealed an interfacial layer of 20–30 nm thickness surrounding parts of the CNTs (Figure 1e). Notably the cast film is over 10 μm thick and does not affect interfacial layer analysis. SEHI which allows for chemical mapping,[34–36] was also applied to confirm the presence of sp^2 carbon for the CNTs and notably highlighted a heterogeneous distribution of chemical bonding in this CNT interfacial layer. SEHI identified chemical bonding variations in SE ranges which have previously been associated with ordered protein structures[37] and S–S (disulfide) bonding. This chemical feature, diagnostic of *B. mori* silk proteins, being present along the length of the CNTs strongly suggests interactions between these two components (Figure 1f). Additional Raman spectroscopy and morphological result also demonstrates a relationship between CNT concentration and protein adsorption (S3–S5, Supporting Information).

Supporting the protein-CNT interaction hypothesis, even after heating solutions to 100 °C and being subjected to strong ultrasonication, this nanoscale interfacial layer still remains on the CNT, suggesting a stabilizing effect. The existence of an interfacial layer may also be inferred from the larger diameter of CNT features revealed in the FIB section of protein-CNT fiber than pristine CNT (S2, Supporting Information). Further heating revealed the protein-CNT layer only disappears after the protein had fully decomposed at ≈275 °C (S2, Supporting Information).

To move beyond electron microscopy based inferences and to elucidate the role of CNTs in silk assembly, synchrotron X-ray ptychotomography was conducted. This advanced technique has been used previously to image pores and changes in electron density (ED) resulting from water loss/uptake in both wool and silk.[38] In this study, it was applied to inspect the necking regions and generate ED maps (**Figure 2**). The longitudinal view in Figure 2a and subsequent sections in Figure 2b–e clearly demonstrate that ED varies substantially with location.

Consistent with the location of Section 1 in the thickest part of the tapered fiber section (closest to the as-spun state), the cross-section map shown in Figure 2b appears relatively uniform and

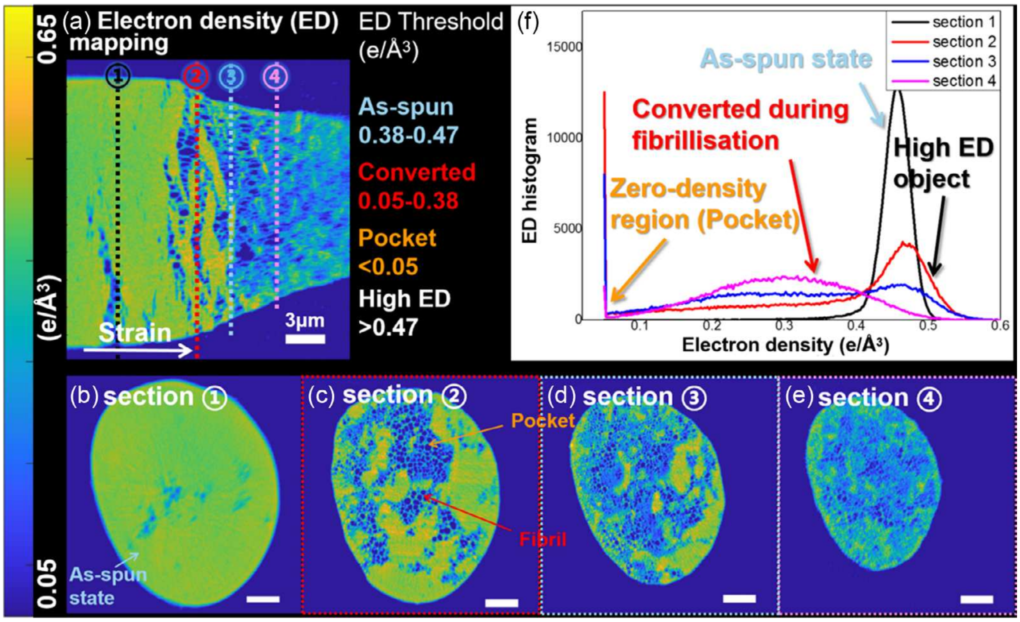

Figure 2. The fibrillization of the silk protein-CNT system is reflected in ED maps. Synchrotron X-ray ptychotomography provided the ED maps throughout the tapered necking site clearly showing a phase separation and transition from as-spun to fibrillized state in longitudinal section. Subsequent cross sections at the 4 points highlighted in a) are presented in b–e). f) The ED histogram comparison of these cross sections. Note the low limit set in this ED mapping is 0.05 e Å^{-3}. The broad peak in the histogram obtained from Section 4 results from structures too small to be resolved fully, which continue to increase in Section 2–4.

with a high average ED. The edge of the fiber appears to have a lower ED, which could indicate that ED values at edges might be affected by the instrument resolution (≈76 nm). Near the center of the fiber, some isolated circular low ED features can be seen.

The cross section at location 2, further along the taper, exhibits very strong inhomogeneity in ED (Figure 2c). In particular, a network of hollow (ED close to zero) structures is present and is consistent with the appearance of pockets within the tapered section as seen above in the FIB/SEM longitudinal section in Figure 1a. A series of high ED objects also emerged along with the pockets, which reflects the emerging of denser nanostructure and would be discussed later in **Figure 3**.

In location 3 (Figure 2d), both fiber diameter and pocket size are reduced further. In fact, some of the pockets have become so small that they cannot be resolved fully. In addition, the number of areas with high ED is reduced. However, within the few remaining areas of high ED round nanostructures with even higher electron densities (almost reaching 0.57) are distinguishable. These nanostructures are still present in the cross section taken at location 4 shown in Figure 2e. However, the average ED is now dominated by structures that cannot be fully resolved due to their small size and thus it appears that they have disappeared.

Regardless of some resolution-related limitations at the thin end of the taper, synchrotron X-ray ptychotomography validates the presence of fibrillar structures of high ED and empty pockets and also highlights their colocalization (Figure 2a). Complete reconstruction of the tapered sections of these fibers is provided in the supplementary multimedia video files. However, in order to understand the causes for these ED variations, some quantification is needed.

For the purpose of quantification, Figure 2f contains histograms that represent the ED values of each pixel in each of the four cross sections. The main peak for the CNT-regenerated silk system in the as-spun state (cross section 1 in Figure 2b) is located at ≈0.44 e Å^{-3}. To put this value into context, the theoretical ED values of silk based on composition and mass density were calculated. Using published data to calculate the value of wet spun silk protein[39] based on the most abundant sequence in *B. mori* fibroin (Gly-Ala-Gly-Ala-Gly-Ser), the calculated ED is 0.444 e Å^{-3}, which is in support of previous observations.

Previous silk and other material hydration X-ray ptychography studies[38,40] also generated histograms from their ED maps. In particular, they noted that a change in position and reduction in height of the protein peak reflected dehydration of the fiber. A similar trend was observed in the histograms across the tapered section of the fiber in Figure 2f, which suggest the loss of water.

A loss of water from silk proteins is often considered a hallmark for the conversion of a disordered silk I conformation to a more crystalline silk II conformation.[41] In tapering systems, this change is supported by an overall increase of β-sheets[42] in the bulk Raman spectra of fibers after the taper (S3, Supporting Information). However, while changes in proteins are identifiable, there is no clear change associated free water peak increase in synchrotron X-ray ptycotomography as one would expect. This is attributed to the fact that the analysis was not carried out immediately after fibers were post drawn, and it can be assumed that free water may have evaporated. It is also considered that fiber aging also caused further water loss occurring on sample surface layer, where yield a slight gradual change of ED in

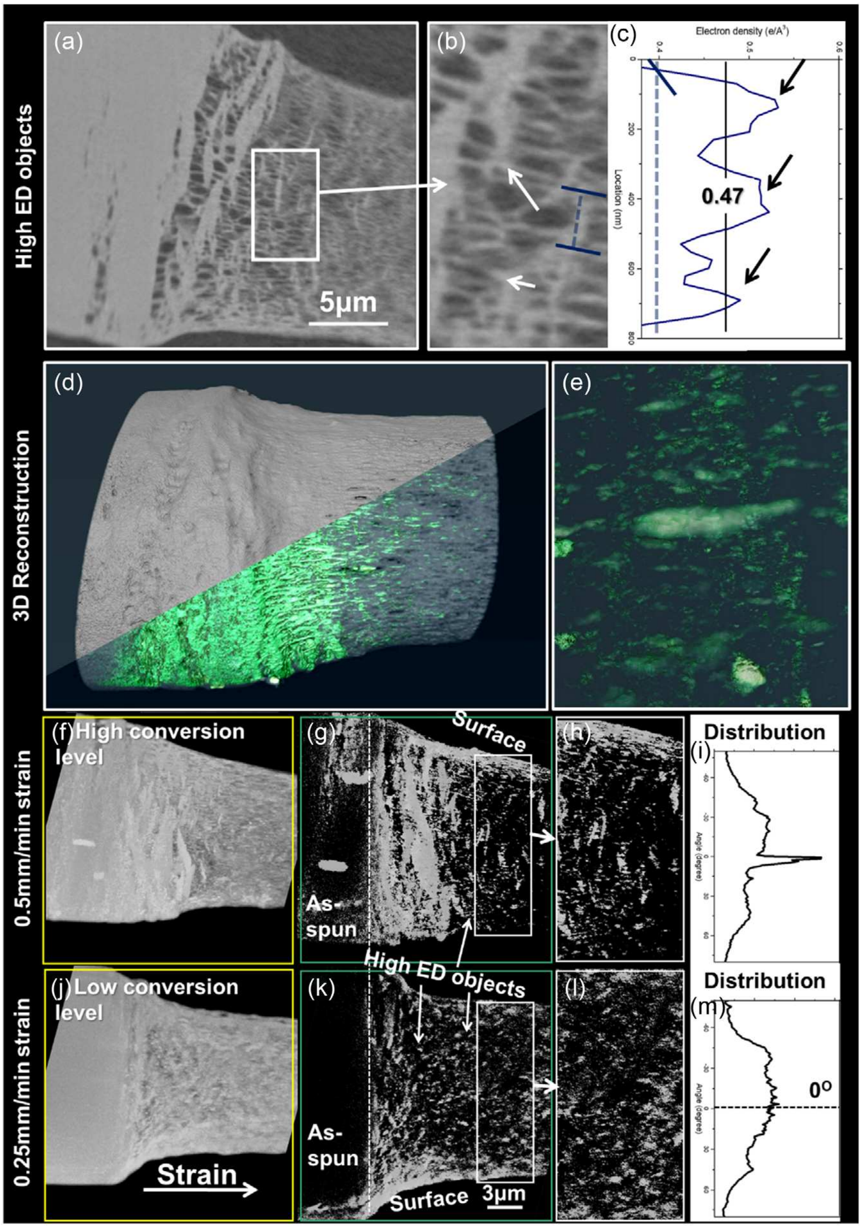

Figure 3. Synchrotron X-ray ptychotomography provided the ED maps throughout the tapered necking site clearly showing a phase separation and transition from as-spun to fibrillized state in longitudinal section (0.5 mm min^{-1} strain). b) A zoomed in view of the region highlighted in a). c) A line profile of the location indicated in (b). d) X-ray ptychography 3D reconstructions of silk (from a) with high ED structures thresholded in green. e) A magnified view of core thresholded nanostructures. f) A projection averaging over a larger volume half the fiber diameter with g,h) containing the high threshold ED distribution. i) Represents the orientation of ED features in (h). j–m) Mirrors the analysis preformed for 0.5 mm min^{-1} strain sample for that of the 0.25 mm min^{-1} strain sample.

Figure 2a (detail discussion in S6, Supporting Information). Nonetheless, it is proposed that a stress-induced phase transition has taken place in the tapering zone due to the presence of (now air-filled) pockets with an ED of zero in the ED histogram (Figure 2f) and observed by FIB-SEM (Figure 1b).

This transformation from less ordered silk I to more crystalline silk II explains the increase of ED up to 0.57 e Å^{-3} in locations where silk content dominates the volumes resolved (>76 nm voxel length). However, if there are smaller amounts of silk in a voxel, the ED is seemingly reduced as each voxel could contain a mix of higher ED silk II and the adjacent zero ED air pockets resulting in an average value of ED that is determined by the proportions of silk and air within each voxel. Thus, instead of a single high ED peak, the converted region after tapering yields a rather broad ED distribution including the average values of crystallized protein, pocket edge region, and CNT seed within the fibrillized structure. This voxel averaging effect also explains the ED drop after conversion, while total electron number (corresponding to material density) remains constant in fiber drawing (details discussed in S6, Supporting Information).

Associating the presence of high ED objects with silk proteins allows us to probe in greater detail the silk protein-CNT system's response to stress induced structure development over greater lengthscales. Silk fibroin in aqueous solutions is widely reported to exist in a silk I conformation as part of micellar structure varying in size from tens to several hundred nanometers[43] (depending on the concentration, pH and measurement techniques). Comparable structures have been previously documented and referred to as nanocompartments[16] in silk in a non-solution state. For clarity in the solid system, the authors favor the term "nanocompartment." The ED maps indicate a transition from silk I to silk II across the tapered fiber section. The organization of nanocompartments may also be discernible if their scale exceeds 76 nm, which is the resolution limit (Figure 3).

Figure 3a visualizes the presence of porous structures across the necking site. Closer inspection (Figure 3b) highlights the confluence of fibrillar structures with low ED pockets (moving left to right across the necking site). The line profile (Figure 3c) is used to establish a suitable threshold of 0.47 e Å^{-3} for high ED structures which is higher than the original "as spun" state of the silk fiber here (0.44 e Å^{-3}). Figure 3d,e presents thresholded tomograms for high ED, revealing circular features on the left of the necking site, which is attributable to nanocompartments. On the right-hand side of the necking site (Figure 3e), elongation of the suspected nanocompartments occurs, with the globular features becoming first aligned and then nanofibrillar "needle-like" structures become positioned within the silk fiber core. A projection averaging over a larger volume half the fiber diameter is shown in Figure 3f, with Figure 3g,h containing the high threshold ED distribution. Figure 3i represents the orientation of ED features in Figure 3h. Dense objects in Figure 3h (0.5 mm min^{-1} sample) follow the orientation of the draw axis and yield an orientation distribution peak of ≈±10°.

Extending this through comparison of tapering sections from fibers that have been drawn under different conditions, Figure 3j–m mirrors the analysis above for a sample drawn at 0.25 mm min^{-1}. At this slower draw rate, there is a lower proportion of ED structures and less overall alignment than in the 0.50 mm min^{-1} drawn sample (Figure 3m). Note both samples are prepared from the same as-spun fiber, the only difference between them is the drawing rate (detail discussed in S7, Supporting Information).

The above findings confirm that higher applied strain rates lead to an increased amount and degree of alignment of high ED structures, which is attributable to proteins in a silk II conformation[44] (S3, Supporting Information), which is supported by numerous bulk spectroscopic measurements.[45,46] Taken together, these observations provide evidence of the process in which nanocompartments convert into silk II nanofibrils aligned with the fiber axis as a result of imposed mechanical stress (a more detailed hypothesis is discussed in S8, Supporting Information).

Further confirmation of the structural transition and alignment over longer length scales comes from optical microscopy (**Figure 4**a). The thick as-spun section of the fiber (left in Figure 4) appears dark when observed with crossed polarizers, whereas the thin part of the fiber appears bright, thus exhibiting clear birefringence and suggesting strong orientation of molecules post draw akin to observations in native silks which have been spun ex vivo.[11] The completeness of structural conversion

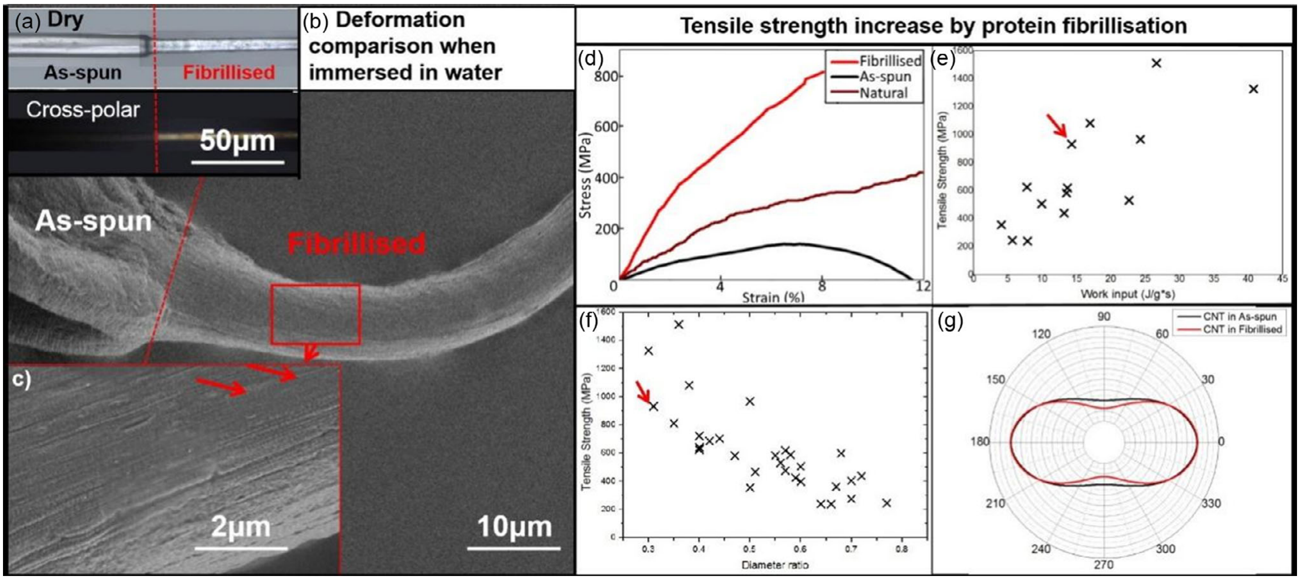

Figure 4. a) Mechanical enhancement of fibrillized composite is decided by silk protein rather than CNT. The construction of fibril structure in silk-CNT fiber is evidenced by a significant optical birefringence increase, similar to silk. b,c) When freely immersed in water, "as-spun silk"-CNT fiber segments swelled and lost their shape, while fibrillized segments retained their structure as displayed in SEM images. d) The strain–stress curve of fibrillized samples are consistent with typical natural silkworm silks, while yielding a tensile strength up to 1 GPa, depending on conditions such as applied strain rate. e) The composite tensile strength can be related to the rate of work input in fibrillization and the ratio of final diameter and initial diameter in fibrillization. f) The data highlighted by the red arrow is the sample presented in the strain–stress curve in (d). g) In contrast, the orientation of CNT is little improved in fibrillization as measured by polarized Raman spectroscopy.

and stability of this system is easily tested in bulk by simply immersing a fiber in flowing water, as silk II structures will not dissolve. It is therefore reported that the as-spun undrawn segments of fibers are almost completely lost, partially redissolving and producing a shrunken appearance, which is in stark contrast to the fibrillized segments which remain well orientated and consolidated (Figure 4b,c).

The final evidence that the inclusion of CNTs facilitates an improved introduction of stress to guide silk protein conversion and fibrillization to form a natural structural hierarchy stems from the mechanical properties of the fibers tested. These are comparable to and even surpasses the properties of naturally spun *B. mori* silk.[47] The Young's modulus and maximum tensile stress of optimized samples reach 15–20 GPa and 650–1100 MPa, respectively (Figure 4d). Overall, the results obtained match previous observations and predictions for both natural and artificial silks; a higher strain work-input-rate and smaller diameter results in stiffer, stronger fibers (Figure 4e,f).[37]

To elucidate what precise roles the inclusion of CNTs may play in the CNT-regenerated silk system presented here and postulate their roles in the conversion of silk the orientation distribution of CNT measured by polarized Raman spectra is shown in Figure 4g before and after fibrillization (further polarized Raman data and analysis in S3 and S4, Supporting Information). Notably, there is very little difference in orientation of the CNTs prior to and after fibrilization and from this it is concluded that any fiber strength enhancement is primarily attributable to the controlled silk protein conversion from silk I to silk II and not the CNTs themselves taking up the load.

Looking into the interaction between these regenerated silk proteins and CNTs, the Amide I band in polarized Raman spectra does not seem to show alignment with the CNTs whereas the protein side changes represented here by Tyrosine do appear to align with the CNTs. Thus, it is proposed Tyrosine is likely to be concentrated in the interfacial layers reported above. Tyrosine's phenol ring has been shown to attach to the sp^2 bonded carbon at the CNT surface via strong π–π interactions[48] and is known to providing templating effects for silk, in particular supporting self-assembly of silk proteins into metastable clusters via π–π interactions which could support larger scale nanocompartment formation and stabilization. In addition, silks' Tyrosine residues[49] are located near C-terminus, which are proposed to contribute towards the hydrophilicity of the nanocompartments' surface. CNT binding in these sites may alter the water binding inside or on the surface of nanocompartments and further affect nanocompartment conversion (detail discussed in S8, Supporting Information). It is tentatively hypothesized that the ability of CNTs to promote and stabilize nanocompartment development in this regenerated silk system enables sufficient localized stress concentrations to develop during draw that permit elongation, fibrillization, and structural conversion of the silk proteins to occur, resulting in improved bulk fiber properties.

3. Conclusion

For the first time, this study reveals an experimentally accessible pathway that allows sufficient control to replicate natural morphologies and match, if not surpass, mechanical properties of natural systems. Specifically, this study utilized CNTs stabilizing interaction with silk to block uncontrolled protein interactions and induce fiber formation through a controlled stress-induced conversion and structure development pathway. Initially, nanoscale structures were confirmed using SEM and SEHI, and, subsequently, synchrotron X-ray ptychotomography was used to capture the fibrillization site cross sections. At this site, the silk phase separates into water pockets, and nanocompartments and elongation into nanofibrils were induced by stress. At the microscale, a combination of optical birefringence and response to hydration supports the hypothesis that protein alignment and denaturation come as a result of an imposed stress field. This provides a theoretical framework for novel processing route exploration, highlighting a new practical means to control self-assembly in silks. Results obtained offer value to the community as it identifies the order and mechanism by which artificial silks can self-assemble to improve fiber mechanical performance. It is envisaged that this model may continue to shed light onto the natural silk formation process and on a wider scale the implemented approach of using carbon nanomaterials to control protein self-assembly pathways to be beneficial to a range of fields, from biomaterials to bioelectronics and green polymers.

4. Experimental Section

Preparation and Processing of Silk-CNT Composite Fiber: The silk protein used in composite fabrication was extracted through a classical "regeneration" process, which has been described in detail in previous research.[15] In brief, *B. mori* silk cocoon was cut into 1 cm^2 pieces and boiled in 1.25% wt citric acid (Sinopharm chemical reagent Co.m AR) to remove silk sericin. This process was repeated twice and then washed with deionized water. Then the silk was dissolved in 60 °C 9.3 mol L^{-1} LiBr (Macklin Shanghai, 99%) water solution for 3 h. The multiwall CNT (J&K Scientific >20 μm length, 20 nm diameter, 99% purity) was dispersed into this silk protein LiBr solution with weight ratio CNT:silk ≈1:100 through ultrasonic treatment. This solution was dialyzed in deionized water for 24 h to remove LiBr (confirmed by silver nitrate titration), and then centrifuged at 8000 rpm rotation rate, 4 °C temperature for 15 min. The supernatant collected was concentrated to ≈24% wt (all solute) through room temperature evaporation. This concentrated silk-CNT solution was transferred to initial fiber preparation. Three samples of 1 mL silk-CNT solution were sealed in centrifuge tubes and boiled in water at 100 °C for 15 min, before used to test the thermo stability of silk-CNT system.

A drop of silk-CNT solution was diluted to 0.01 wt% in deionized water and spin cast on a 1 cm^2 silicon substrate at spin rate 1200 rpm min^{-1} for 3 min. This cast sample represents the state of silk-CNT interaction before fiber spinning and was stored for characterization.

A fine needle tip was dipped into the concentrated silk-CNT solution and then pulled up in air using a universal mechanical testing machine at ≈1 mm s^{-1} speed forming the initial as-spun fiber. The as-spun fiber was collected and cut into ≈10 mm long segments and further drawn down by universal testing machine with drawn rate 0.1–2 mm min^{-1} as shown in Figure 1. The drawn composite fiber was collected and used in testing and analysis. More details regarding the sample collection are provided in S7, Supporting Information. All processing was done at room temperature and ≈35% humidity. The mechanical properties of the samples are tested under adjusted conditions of same room humidity afterward. One group of fiber samples was strained between two steel pillars and heated in a muffle furnace to test material stability when protein oxidizes in air. The furnace temperature was raised by 15 °C every 10 min until 275 °C, then this temperature was maintained for 60 min before slowly air cooling to room temperature.

Morphological Analysis and Imaging Techniques: The composite fiber samples were imaged using an FEI Nova 450 SEM. Backscattered images (contrast based on local atom number and mass density) were collected in order to locate CNT in composite sections. The imaging was done at 1 keV primary electron energy and conductive coating was avoided. Longitudinal sections of composite fiber were prepared using a FEI Helios focus ion beam (FIB) SEM. The material in the fiber was removed slice by slice under the ion beam radiation, until the longitudinal section in central region of fiber was revealed. The composite fiber segment with the FIB cut window was collected and stored for other characterization.

The secondary electron spectra of silk-CNT system were collected using a FEI Helios SEM. The detail of spectra collection and SEHI has been demonstrated in previous studies[36,50,51] SEHI data collection of spin cast silk-CNT sample was performed using the Helios Nanolab G3 UC microscope. This was conducted by applying known operating conditions of 1 kV (monochromated) and 50 pA immersion mode (mode II/UHR[35]). To ensure that SEHI images captured were taken of the actual material surface, no conductive coating deposition was applied to the samples in contrast to conventional SEM analysis. The collection of SES/SEHI of different energy ranges was achieved through the adjustment of the mirror electrode voltage (MV) together with a tube bias setting of 150 V. Stepping the MV in a range of −15 and 15 V (energy range of −0.7 to 12.7 eV) was achieved through the use of an automatic iFast collection recipe.[52] Every image was collected at a frame interval of 0.5 s and an MV step size of 0.5 V, which corresponds to ≈0.2 eV electron energy step size. Image processing was undertaken using Fiji Image J software (ImageJ2, open-source). SEHI data were obtained by differentiating the captured S curves. Isolating components of interest was attained by performing component analysis of the image stacks through nonnegative matrix factorization. In brief, SEHI image contrast of pixels on SE image is proportional to SE signal intensity. This chemical mapping is compared to morphological data is conventional SEM imaging to identify silk-CNT nano structures.

Orientation Characterization: The overall orientation of silk-CNT composite fiber was characterized by polarized Raman spectroscopy using a Witec Alpha300R-2018 spectrometer. The composite fiber was fixed on glass substrate and aligned to a polarizer at the start of Raman spectra collection. The spectra were collected using 0.4 W 570 nm laser with radiation time 0.1 s and repeated for 100 times to reduce noise. The polarized spectra were collected on fiber direction 0°, 30°, 60°, and 90° versus the polarizer. Each group of spectra was collected for as-spun and fibrillized segment of a single composite fiber to avoid any chemical composition difference.

X-ray Data Acquisition and Processing: The X-ray 3D tomograms were recorded using ptychographic tomography. The experiments were performed at the coherence branch I13-1 beamline of the Diamond Light Source (Oxford, UK).[53–55] A monochromatic beam with an energy of 9.7 keV was focused via a Fresnel zone plate, and the sample was positioned slightly downstream of the focal plane to have a beam spot size of 4 μm on it. For each ptychographic projection, a 2D raster scan of 100×40 ($H \times V$) positions with step sizes of 330 nm × 660 nm was performed and a continuous scanning mode was used along the horizontal direction. The diffraction patterns were recorded with an Eiger detector of 1030×514 pixels (pixel size 75 μm) at a sample to detector distance of 4.9 m with an exposure time of 5 ms. The X-ray flux is 2×10^8 photons s^{-1}. A total of 1000 projections were measured with equal angular spacing covering an angular range of 180° over about 8 h. The radiation damage done in measuring process is tested by comparing the start and end projection image. Correlation between 0° and 180° showed no observable radiation damage (detail shown in S6, Supporting Information).

Ptychographic reconstructions were undertaken with an in-house package based on the ePIE algorithm[56] for each projection. A cropped detector region of 396×396 pixels was used (giving a pixel size of 21 nm), and 300 iterations were run. Three probe modes and positional correction were used to clean the reconstructions. For each of these 2D projection reconstructions, the complex object transmission function contains both the amplitude and phase shift information. Then with the phase shift information, all the projections were unwrapped, aligned, and reconstructed using the open-sourced MATLAB package[54,55] developed by cSAXS beamline at Paul Scherrer Institute (PSI),[57] to give the final 3D tomograms. The ED (e Å^{-3}) was then calculated from the phase tomograms using the relation as described elsewhere.[58]

Supporting Information

Supporting Information is available from the Wiley Online Library or from the author.

Acknowledgements

The authors thank The Royal Society and National Natural Science Foundation of China for funding through the Royal Society-Newton Mobility Grant (IEC\NFSC\181308 and NFSC-81911530223). The authors thank Diamond Light Source for beamtime (proposal MG28729-1) and the staff of beamlines I13 for assistance with sample preparation, optical setup alterations, and data collection. C.R. thanks EPSRC for support under EP/N008065/1 and EP/V012126/1. C.H. thanks EPSRC for support under EP/K005693/1. NF thanks EPSRC for support under EP/T517835/1. M.Y. thanks for support by the following funding bodies: NSFC (31 800 807), Zhejiang Provincial Natural Science Foundation of China (LZ17C170002), State of Sericulture Industry Technology System (CARS-18-ZJ0501), Fundamental Research Funds for the Central Universities (2018XZZX001-11), Zhejiang Provincial Science and Technology Plans (2016C02054-19), and Zhejiang Provincial Key Laboratory of Utilization and Innovation of Silkworm and Bee Resources (2020E10025). Q.W. thank Zhejiang Province Natural Science Foundation for support under LQ23E030011. The authors thank Sorby Centre, University of Sheffield and CCEM, Zhejiang University for assistance with microscopy analysis. Q.W. thank Dr Minjie Zhang of Prof Yi Zheng group, Zhejiang University for assistance with Raman spectroscopy.

Conflict of Interest

The authors declare no conflict of interest.

Data Availability Statement

The data that support the findings of this study are available from the corresponding author upon reasonable request.

Keywords

biomaterials, hierarchical structure, nano-materials, post-spin draw, X-ray tomography

Received: December 12, 2023
Published online:

---

[1] D. Ji, Y. Bin Deng, P. Zhou, *J. Mol. Struct.* **2009**, *938*, 305.
[2] H. Sun, B. Marelli, *Nat. Commun.* **2020**, *11*, 351.
[3] A. Koeppel, N. Stehling, C. Rodenburg, C. Holland, *Adv. Funct. Mater.* **2021**, *31*, 2103295.
[4] S. Sampath, T. Isdebski, J. E. Jenkins, J. V. Ayon, R. W. Henning, J. P. R. O. Orgel, O. Antipoa, J. L. Yarger, *Soft Matter* **2012**, *8*, 6713.
[5] M. Frydrych, A. Greenhalgh, F. Vollrath, *Sci. Rep.* **2019**, *9*, 15428.
[6] L. Liu, X. Yang, H. Yu, C. Ma, J. Yao, *RSC Adv.* **2014**, *4*, 14304.

[7] M. Sun, Y. Zhang, Y. Zhao, H. Shao, X. Hu, *J. Mater. Chem.* **2012**, *22*, 18372.
[8] S. H. Kim, Y. S. Nam, T. S. Lee, W. H. Park, *Polym. J.* **2003**, *35*, 185.
[9] K. Spiess, A. Lammel, T. Scheibel, *Macromol. Biosci.* **2010**, *10*, 998.
[10] I. C. Um, C. S. Ki, H. Y. Kweon, K. G. Lee, D. W. Ihm, Y. H. Park, *Int. J. Biol. Macromol.* **2004**, *34*, 107.
[11] N. Weatherbee-Martin, L. Xu, A. Hupe, L. Kreplak, D. S. Fudge, X. Q. Liu, J. K. Rainey, *Biomacromolecules* **2016**, *17*, 2737.
[12] E. M. Campo, D. Yates, B. Berson, W. Rojas, A. D. Winter, M. Ananth, J. J. Santiago-Aviles, E. M. Terentjev, *Macromol. Mater. Eng.* **2017**, *302*, 1600479.
[13] R. C. Masters, N. Stehling, K. J. Abrams, V. Kumar, M. Azzolini, N. M. Pugno, M. Dapor, A. Huber, P. Schäfer, D. G. Lidzey, C. Rodenburg, *Adv. Sci.* **2019**, *6*, 1801752.
[14] M. Dierolf, A. Menzel, P. Thibault, P. Schneider, C. M. Kewish, R. Wepf, O. Bunk, F. Pfeiffer, *Nature* **2010**, *467*, 436.
[15] Q. Wan, M. Yang, J. Hu, F. Lei, Y. Shuai, J. Wang, C. Holland, C. Rodenburg, M. Yang, *Nat. Commun.* **2021**, *12*, 3711.
[16] D. Eliaz, S. Paul, D. Benyamin, A. Cernescu, S. R. Cohen, I. Rosenhek-Goldian, O. Brookstein, M. E. Miali, A. Solomonov, M. Greenblatt, Y. Levy, U. Raviv, A. Barth, U. Shimanovich, *Nat. Commun.* **2022**, *13*, 7856.
[17] L. Valentini, S. Bittolo Bon, M. Tripathi, A. Dalton, N. M. Pugno, *Front. Mater.* **2019**, *6*, 60.
[18] E. Lepore, F. Bosia, F. Bonaccorso, M. Bruna, S. Taioli, G. Garberoglio, A. C. Ferrari, N. M. Pugno, *2D Mater.* **2017**, *4*, 031013.
[19] S. P. Kelly, K. P. Huang, C. P. Liao, R. A. N. Khasanah, F. S. Sen Chien, J. S. Hu, C. L. Wu, I. M. Tso, *PLoS One* **2020**, *15*, 0241829.
[20] X. Zhang, A. L. Licon, T. I. Harris, P. F. Oliveira, B. J. McFarland, B. E. Taurone, B. J. Walsh, B. E. Bell, C. T. Walker, R. V. Lewis, J. A. Jones, *ACS Omega* **2019**, *4*, 4832.
[21] H. Xu, W. Yi, D. Li, P. Zhang, S. Yoo, L. Bai, J. Hou, X. Hou, *RSC Adv.* **2019**, *9*, 3558.
[22] L. Ma, M. A. Akurugu, V. Andoh, H. Liu, J. Song, G. Wu, L. Li, *Sci. China Mater.* **2019**, *62*, 245.
[23] S. Ling, Q. Wang, D. Zhang, Y. Zhang, X. Mu, D. L. Kaplan, M. J. Buehler, *Adv. Funct. Mater.* **2018**, *28*, 1705291.
[24] G. R. Plaza, P. Corsini, J. Pérez-Rigueiro, E. Marsano, G. V. Guinea, M. Elices, *J. Appl. Polym. Sci.* **2008**, *109*, 1793.
[25] G. J. G. Davies, D. P. Knight, F. Vollrath, *Tissue Cell* **2013**, *45*, 306.
[26] J. Sparkes, C. Holland, *Macromol. Biosci.* **2019**, *19*, 1800229.
[27] J. Péreź-Rigueiro, C. Viney, J. Llorca, M. Elices, *J. Appl. Polym. Sci.* **1998**, *70*, 2439.
[28] H. J. Jin, D. L. Kaplan, *Nature* **2003**, *424*, 1057.
[29] P. Poza, J. Pérez-Rigueiro, M. Elices, J. LLorca, *Eng. Fract. Mech.* **2002**, *69*, 1035.
[30] T. Y. Lin, H. Masunaga, R. Sato, A. D. Malay, K. Toyooka, T. Hikima, K. Numata, *Biomacromolecules* **2017**, *18*, 1350.
[31] A. D. Malay, H. C. Craig, J. Chen, N. A. Oktaviani, K. Numata, *Biomacromolecules* **2021**, *23*, 1827.
[32] S. K. Siddiquee, P. J. Willcox, J. W. Van Egmond, S. P. Gido, *Macromolecules* **1997**, *30*, 5372.
[33] A. Koeppel, P. R. Laity, C. Holland, *Soft Matter* **2018**, *14*, 8838.
[34] N. T. H. Farr, S. Roman, J. Schäfer, A. Quade, D. Lester, V. Hearnden, S. Macneil, C. Rodenburg, *RSC Adv.* **2021**, *11*, 34710.
[35] N. T. H. Farr, B. Klosterhalfen, G. K. Noé, *J. Biomed. Mater. Res., Part B* **2023**, *111*, 1142.
[36] N. Farr, J. Thanarak, J. Schäfer, A. Quade, F. Claeyssens, N. Green, C. Rodenburg, *Adv. Sci.* **2021**, *8*, 2003762.
[37] N. Stehling, K. J. Abrams, C. Holland, C. Rodenburg, *Front. Mater.* **2019**, *5*, 84.
[38] M. Esmaeili, J. B. Fløystad, A. Diaz, K. Høydalsvik, M. Guizar-Sicairos, J. W. Andreasen, D. W. Breiby, *Macromolecules* **2013**, *46*, 434.
[39] K. Sen, M. Babu K, *J. Appl. Polym. Sci.* **2004**, *92*, 1116.
[40] G. Geng, R. J. Myers, Y. S. Yu, D. A. Shapiro, R. Winarski, P. E. Levitz, D. A. L. Kilcoyne, P. J. M. Monteiro, *Cem. Concr. Res.* **2018**, *111*, 130.
[41] A. Percot, P. Colomban, C. Paris, H. M. Dinh, M. Wojcieszak, B. Mauchamp, *Vib. Spectrosc.* **2014**, *73*, 79.
[42] S. Sohn, H. H. Strey, S. P. Gido, *Biomacromolecules* **2004**, *5*, 751.
[43] P. Chen, H. S. Kim, C. Y. Park, H. S. Kim, I. J. Chin, H. J. Jin, *Macromol. Res.* **2008**, *16*, 539.
[44] C. Holland, K. O'Neil, F. Vollrath, C. Dicko, *Biopolymers* **2012**, *97*, 368.
[45] R. J. Young, C. Holland, Z. Shao, F. Vollrath, *MRS Bull.* **2021**, *46*, 915.
[46] M. M. R. Khan, H. Morikawa, Y. Gotoh, M. Miura, Z. Ming, Y. Sato, M. Iwasa, *Int. J. Biol. Macromol.* **2008**, *42*, 264.
[47] S. Chen, M. Liu, H. Huang, L. Cheng, H. P. Zhao, *Mater. Des.* **2019**, *181*, 108077.
[48] X. Liang, H. Li, J. Dou, Q. Wang, W. He, C. Wang, D. Li, J. M. Lin, Y. Zhang, *Adv. Mater.* **2020**, *32*, 2000165.
[49] P. Partlow, M. Bagheri, J. L. Harden, D. L. Kaplan, *Biomacromolecules* **2016**, *17*, 3570.
[50] N. Farr, S. Pashneh-Tala, N. Stehling, F. Claeyssens, N. Green, C. Rodenburg, *Macromol. Rapid Commun.* **2020**, *41*, 1900484.
[51] N. T. H. Farr, S. F. Hamad, E. Gray, C. M. Magazzeni, F. Longman, D. E. J. Armstrong, J. P. Foreman, F. Claeyssens, N. H. Green, C. Rodenburg, *Polym. Chem.* **2021**, *12*, 177.
[52] N. T. H. Farr, G. M. Hughes, C. Rodenburg, *Materials* **2021**, *14*, 3034.
[53] C. Rau, M. Storm, S. Marathe, A. J. Bodey, S. Cipiccia, D. Batey, X. Shi, M. C. Zdora, I. Zanette, in *AIP Conf. Proc.*, Woodbury, New York, US **2019**.
[54] M. Odstrčil, M. Holler, J. Raabe, M. Guizar-Sicairos, *Opt. Express* **2019**, *27*, 36637.
[55] M. Guizar-Sicairos, A. Diaz, M. Holler, M. S. Lucas, A. Menzel, R. A. Wepf, O. Bunk, *Opt. Express* **2011**, *19*, 21333.
[56] A. M. Maiden, J. M. Rodenburg, *Ultramicroscopy* **2009**, *109*, 1256.
[57] X. Wei, P. Urbach, *Opt. Express* **2019**, *27*, 36767.
[58] A. Diaz, P. Trtik, M. Guizar-Sicairos, A. Menzel, P. Thibault, O. Bunk, *Phys. Rev. B: Condens. Matter Mater. Phys.* **2012**, *85*, 020104.